Environmetrics 00, 1–26

DOI: 10.1002/env.XXXX

Nonlinear reaction-diffusion process models improve inference for population dynamics

Xinyi Lu[1*] Perry J. Williams[2], Mevin B. Hooten[3,1], James A. Powell[4], Jamie N. Womble[5,6], and Michael R. Bower[5]

Summary: Partial differential equations (PDEs) are a useful tool for modeling spatio-temporal dynamics of ecological processes. However, as an ecological process evolves, we need statistical models that can adapt to changing dynamics as new data are collected. We developed a model that combines an ecological diffusion equation and logistic growth to characterize colonization processes of a population that establishes long-term equilibrium over a heterogeneous environment. We also developed a homogenization strategy to statistically upscale the PDE for faster computation and adopted a hierarchical framework to accommodate multiple data sources collected at different spatial scales. We highlighted advantages of using a logistic reaction component instead of a Malthusian component when population growth demonstrates asymptotic behavior. As a case study, we demonstrated that our model improves spatio-temporal abundance forecasts of sea otters in Glacier Bay, Alaska. Further, we predicted spatially-varying local equilibrium abundances as a result of environmentally-driven diffusion and density-regulated growth. Integrating equilibrium abundances over the study area in our application enabled us to infer the overall carrying capacity of sea otters in Glacier Bay, Alaska.

Keywords: Fokker-Planck Equation · Homogenization · Spatio-temporal Process · State-Space Model

[1] *Department of Statistics, Colorado State University, Fort Collins, Colorado 80523 USA*
[2] *Department of Natural Resources and Environmental Science, University of Nevada, Reno, Nevada 89557 USA*
[3] *U.S. Geological Survey, Colorado Cooperative Fish and Wildlife Research Unit, Department of Fish, Wildlife, and Conservation Biology, Colorado State University, Fort Collins, Colorado 80523 USA*
[4] *Department of Mathematics and Statistics, Utah State University, Logan, UT 84322 USA*
[5] *Southeast Alaska Inventory and Monitoring Network, National Park Service, 3100 National Park Rd, Juneau, Alaska 99801 USA*
[6] *Glacier Bay Field Station, National Park Service, 3100 National Park Rd, Juneau, Alaska 99801 USA*
[*] *Correspondence to: X. Lu, email: luxinyi@colostate.edu*

This paper has been submitted for consideration for publication in *Environmetrics*

1. INTRODUCTION

The dynamics of ecological systems are complicated because the interaction between organisms and their host environment may vary in space and time. Traditionally, generalized linear mixed models (GLMM) have been favored to describe spatio-temporal ecological processes (e.g., Banerjee et al., 2004). While such models enjoy a relatively large degree of flexibility, they lack an explicit mechanistic interpretation of the underlying process. Moreover, conventional GLMMs are often incapable of capturing the joint spatio-temporal dependence that is characteristic of ecological processes (Wikle and Hooten, 2010). On the other hand, mechanistic statistical models are increasingly popular because they allow us to formally incorporate our knowledge of the system we seek to understand in latent processes (Hilborn and Mangel, 1997). In particular, partial differential equations (PDEs) have been commonly used to represent ecological processes due to their connections to physical laws (Wikle, 2003; Cressie and Wikle, 2011). By embedding the PDEs in a hierarchical framework, we can appropriately account for uncertainty in the data, our prior understanding of the process, and parameters that influence the process (Berliner, 1996; Hobbs and Hooten, 2015).

In what follows, we present a hierarchical reaction-diffusion model that was motivated by the case study of sea otter colonization in Glacier Bay, Alaska. Across their North Pacific range, sea otter populations have undergone significant fluctuations over the past two centuries. After being hunted to near extirpation during the maritime fur trade, 13 remnant colonies remained, and sea otter populations have subsequently recovered in many areas due to a combination of conservation efforts and environmental changes (Larson et al., 2014). In 1988, sea otters were first documented at the mouth of Glacier Bay, and have expanded throughout much of the bay. The study of sea otter colonization in Glacier Bay provides important insight into the ability of a species to recover from near extirpation, as well as the impact of a changing climate on their recovery (Williams et al., 2019).

Reaction-diffusion models have long been used to describe the colonization or invasion of

a species (e.g., Holmes et al., 1994). Past studies of reaction-diffusion models in a statistical framework have focused on development of a spatially dynamic diffusion component, while relying on a relatively simple reaction term (Wikle, 2003; Hooten and Wikle, 2008; Zheng and Aukema, 2010; Williams et al., 2017). A commonly used model for reaction, the Malthusian growth model, assumes that the per capita growth rate remains the same regardless of population size (Turchin, 2003). This may be reasonable at initial stages of a colonization, but as the species expands into the environment, the population can become resource-limited, resulting in a decline in growth rate. Recently collected data indicate a slowing of sea otter expansion in Glacier Bay; thus, we adopted a reaction model based on logistic growth that assumes the per capita growth rate declines as the population size approaches a maximum (i.e., carrying capacity) regulated by the amount of available resources. Logistic growth is more realistic in characterizing population growth during colonization, and allows us to gain insight about the system at its equilibrium. For example, we may learn about the spatially-varying equilibrium abundances over a heterogeneous environment, as well as the overall carrying capacity of the environment with associated uncertainty.

Fitting statistical reaction-diffusion models can be computationally challenging when the scale of the process is fine in space and/or time. The approach we present induces computational economy via the mathametical technique of homogenization. Using the "method of multiple scales" (Holmes, 2013; Garlick et al., 2011), our implementation relies on a solution to the PDE at a larger spatial scale, while maintaining the inference on parameters at the original small scale (Hooten et al., 2013).

Furthermore, our method is useful for reconciling multiple data sources collected at different spatial scales with varying degrees of accuracy. In our application, inconsistency in spatial scales comes partly from improvements in aerial survey technology over time. Our modeling framework is compatible with both the past and the more recent survey methodology for monitoring sea otters in Glacier Bay, and is therefore useful for inference and forecasting

based on ongoing data collection efforts.

The rest of the paper proceeds as follows. In section two, we develop a hierarchical model and demonstrate that a homogenized reaction-diffusion process reduces computational complexity. In section three, we illustrate the model through simulation and the sea otter case study, thereby showing that the logistic reaction component improves parameter inference and population forecast compared to the Malthusian reaction component. Finally, in section four, we conclude the paper with a discussion of possible extensions and broader applications of our model.

2. METHODS

2.1. Hierarchical Model

2.1.1. Data Model

The goal of our model is to infer sea otter abundance in continuous space and time within our study area given observed data on relative abundances at a subset of locations and time points, and true abundances observed at a subsequent subset of locations and time points. We let $y_{i,t}$ denote the observed relative abundance of sea otters at a site $\mathcal{S}_i$ in year t. Following the N-mixture framework (Royle, 2004), we modeled the relative abundance using a binomial distribution conditioned on (latent) site-specific true abundance, $N_{i,t}$, and detection probability, p_t, as follows,

$$y_{i,t} \sim \text{Binom}\left(N_{i,t},\ p_t\right). \tag{1}$$

2.1.2. Process Model

We modeled the latent, true abundance, $N_{i,t}$, using a negative binomial distribution conditioned on a dynamically evolving mean (population intensity), $\lambda_{i,t}$, and dispersion

parameter τ, thereby providing the process model with more flexibility than other commonly used count models, such as the Poisson model (Ver Hoef and Boveng, 2007). Population intensity $\lambda(\boldsymbol{s}, t)$ with $\boldsymbol{s} \equiv (s_1, s_2)'$ is modeled in continuous space and time, where integration over a site $\mathcal{S}_i$ results in the mean abundance $\lambda_{i,t}$. Assuming conditional independence of latent, true abundances given population intensities, we have

$$N_{i,t} \sim \text{NB}\left(\lambda_{i,t},\ \tau\right), \tag{2}$$

$$\lambda_{i,t} = \int_{\mathcal{S}_i} \lambda(\boldsymbol{s}, t) d\boldsymbol{s}. \tag{3}$$

We then modeled the spatio-temporal dynamics of population intensities with the following reaction-diffusion equation,

$$\frac{\partial}{\partial t}\lambda(\boldsymbol{s}, t) = \underbrace{\left(\frac{\partial^2}{\partial s_1^2} + \frac{\partial^2}{\partial s_2^2}\right)\delta(\boldsymbol{s})\lambda(\boldsymbol{s}, t)}_{\textbf{(i)}} + \underbrace{\gamma\lambda(\boldsymbol{s}, t)\left(1 - \frac{\lambda(\boldsymbol{s}, t)}{K}\right)}_{\textbf{(ii)}}. \tag{4}$$

The diffusion component in **(i)** of Equation 4 is known as a Fokker-Planck equation (Risken, 1989), and can be derived from individual movement processes following the convention of Turchin (1998). The diffusion coefficients, $\delta(\boldsymbol{s})$, also known as motility coefficients, are inversely related to residence time (Turchin, 1998; Hooten et al., 2013). With $\delta(\boldsymbol{s})$ inside the second derivative, the Fokker-Planck equation allows population intensity to vary sharply between neighboring locations at the transition of habitat types (Garlick et al., 2011; Hooten et al., 2013; Hefley et al., 2017), which is useful for capturing the variability in sea otter intensity due to their resting and foraging behaviors in different environments. We modeled heterogeneity in diffusion coefficients as a log-linear function of a set of environmental covariates such that $\log(\delta(\boldsymbol{s})) = \boldsymbol{x}(\boldsymbol{s})'\boldsymbol{\beta}$, where $\boldsymbol{x}(\boldsymbol{s})$ is a vector of ocean depth (indicator of < 40 m), distance to shore, slope of the ocean floor, and shoreline complexity (Williams et al., 2017).

The reaction component in **(ii)** of Equation 4 is modeled after logistic growth, where γ

is the parameter for intrinsic growth rate and K is the local density-dependent parameter regulating growth. We let the parameters γ and K be constant in space and time. Although it is possible to model them as variable in space, heterogeneity in both the diffusion and the reaction components may be unidentifiable. In what follows, we illustrate that although a single parameter K is used to regulate growth, the resulting equilibrium abundances in our study system are spatially heterogeneous due to the changing balance between ecological diffusion and density dependence.

We used a scaled Gaussian kernel for the initial conditions of Equation 4,

$$\lambda(\boldsymbol{s}, t_0) = \frac{\theta \exp\left(\frac{-|\boldsymbol{s}-\boldsymbol{s}_d|^2}{\kappa^2}\right)}{\int_{\mathcal{S}} \exp\left(\frac{-|\boldsymbol{s}-\boldsymbol{s}_d|^2}{\kappa^2}\right) d\boldsymbol{s}}, \tag{5}$$

where θ controls the magnitude of initial population intensity, and κ controls the initial population range. The location $\boldsymbol{s}_d = (s_{1d}, s_{2d})'$ is an epicenter fixed to be near the mouth of Glacier Bay, where sea otters were observed before the colonization initiated. The starting time t_0 was chosen to be year 1993 when the earliest data were collected. Following the example by Williams et al. (2017), we used a no-flux spatial boundary condition (Cantrell and Cosner, 2004) at locations adjacent to land, so that diffusive movement onto land will be reflected back to water at such boundaries. We also assumed the study system is closed to immigration because sea otters are protected inside the National Park, but not necessarily outside.

2.1.3. Parameter Model

To complete the model hierarchy, we specified prior distributions for the data and process model parameters. We used a uniform prior from 0 to 0.5 for intrinsic growth rate, γ, because we had sufficient evidence that the population was expanding during the study period, and

the study by Estes (1990) estimated the maximum reproductive rate of sea otters in south-east Alaska to range from 0.196 to 0.237. We used a beta prior centered at 0.75 for the detection probabilities, p_t, as informed by previous studies (Williams et al., 2017). The rest of the parameters were given vague priors. A full description of prior specifications can be found in Appendix A.

The joint posterior distribution associated with our model is

$$\begin{aligned}[\boldsymbol{N}_u, \boldsymbol{p}, \tau, \boldsymbol{\beta}, \theta, \kappa, \gamma, K | \boldsymbol{Y}, \boldsymbol{N}_o] \propto & \left\{ \prod_{i=1}^{n_t} \prod_{t=1}^{T} [y_{i,t} | N_{i,t}, p_t] \right\} \\ & \times \left\{ \prod_{j=1}^{n_t - n_{o,t}} \prod_{t=1}^{T} [N_{j,t} | \boldsymbol{\beta}, \theta, \kappa, \gamma, K, \tau] \right\} \\ & \times [\boldsymbol{p}][\tau][\boldsymbol{\beta}][\theta][\kappa][\gamma][K][\tau], \end{aligned} \tag{6}$$

where $\boldsymbol{N}_o$ denotes the vector of observed true abundances, and $\boldsymbol{N}_u$ denotes the vector of unobserved true abundances that are modeled as latent variables. We let n_t represent the total number of sites where relative abundance was observed in year t, and $n_{o,t}$ represent the number of sites where true abundance was observed in year t.

2.2. Homogenization

When the spatial domain is large and the spatial resolution is fine, solving Equation 4 repeatedly can be computationally demanding. The concept of homogenization is to rewrite Equation 4 in terms of both large and small spatial scales, so that, under certain approximation conditions, we can solve the PDE numerically at the large scale and recover the small scale solutions through a downscaling transformation.

Suppose the diffusion coefficient, δ, depends on two spatial scales, varying quickly on a small spatial scale, and much more slowly on a large spatial scale. We let $\boldsymbol{s}$ denote the fine grain spatial variable in two-dimensions, and introduce the coarse grain spatial variable

$\boldsymbol{\omega} \equiv (\omega_1, \omega_2)'$. Suppose $\boldsymbol{\omega} = \boldsymbol{s}\epsilon$, where $0 < \epsilon \ll 1$ is the ratio between the two scales, such that changes on the order of $\mathcal{O}(\epsilon)$ in $\boldsymbol{\omega}$ become changes on the order of $\mathcal{O}(1)$ in $\boldsymbol{s}$ (Powell and Zimmermann, 2004). Although there have not been individual-level movement studies of sea otters in Glacier Bay, in our application, we assumed sea otters exhibit relatively high site-fidelity and daily movements on the scale of hundreds of meters based on studies from other areas (e.g., Jameson, 1989), whereas the available environmental covariates in Glacier Bay vary on the scale of kilometers, which indicates that $\epsilon \approx 1/10$. In addition, we let t denote the temporal variable associated with $\boldsymbol{\omega}$. We consider Equation 4, which we outline below as a reminder,

$$\frac{\partial \lambda}{\partial t} = \left(\frac{\partial^2}{\partial s_1^2} + \frac{\partial^2}{\partial s_2^2} \right) \delta\lambda + \gamma\lambda \left(1 - \frac{\lambda}{K} \right).$$

By transforming derivatives on the spatial variables in each dimension, $\frac{\partial^2}{\partial s_i^2} \rightarrow \frac{1}{\epsilon^2}\frac{\partial^2}{\partial s_i^2} + \frac{2}{\epsilon}\frac{\partial^2}{\partial s_i \partial \omega_i} + \frac{\partial^2}{\partial \omega_i^2}$, $i = 1, 2$, and writing λ as a power series in ϵ, $\lambda = \lambda_0 + \epsilon\lambda_1 + \epsilon^2\lambda_2 + \cdots$, we obtain the following PDE,

$$\epsilon^2 \frac{\partial}{\partial t}\left(\lambda_0 + \epsilon\lambda_1 + \epsilon^2\lambda_2 + \cdots\right) = \left[\frac{\partial^2}{\partial s_1^2} + \frac{\partial^2}{\partial s_2^2} + 2\epsilon\left(\frac{\partial^2}{\partial s_1 \partial \omega_1} + \frac{\partial^2}{\partial s_2 \partial \omega_2} \right) + \epsilon^2 \left(\frac{\partial^2}{\partial \omega_1^2} + \frac{\partial^2}{\partial \omega_2^2} \right) \right] \times$$
$$\left[\delta\left(\lambda_0 + \epsilon\lambda_1 + \epsilon^2\lambda_2 + \cdots\right)\right] + \epsilon^2\gamma\left(\lambda_0 + \epsilon\lambda_1 + \epsilon^2\lambda_2 + \cdots\right)\left[1 - \frac{\lambda_0 + \epsilon\lambda_1 + \epsilon^2\lambda_2 + \cdots}{K}\right].$$

Gathering terms of $\mathcal{O}(\epsilon^0)$, we have $0 = \left(\frac{\partial^2}{\partial s_1^2} + \frac{\partial^2}{\partial s_2^2} \right) \delta\lambda_0$, which implies $\delta\lambda_0 = C_0(\boldsymbol{\omega}, t)$. Gathering terms of $\mathcal{O}(\epsilon^1)$, we have $0 = \left(\frac{\partial^2}{\partial s_1^2} + \frac{\partial^2}{\partial s_2^2} \right) \delta\lambda_1$. Because λ_1 satisfies the same equation as λ_0, no new information is provided, and without loss of generality we let $\lambda_1 = 0$ (Garlick et al., 2011). Finally, gathering terms of $\mathcal{O}(\epsilon^2)$, we have

$$\frac{1}{\delta}\frac{\partial}{\partial t} C_0(\boldsymbol{\omega}, t) = \left(\frac{\partial^2}{\partial s_1^2} + \frac{\partial^2}{\partial s_2^2} \right)(\delta\lambda_2) + \left(\frac{\partial^2}{\partial \omega_1^2} + \frac{\partial^2}{\partial \omega_2^2} \right) C_0(\boldsymbol{\omega}, t) + \gamma \frac{C_0(\boldsymbol{\omega}, t)}{\delta}\left(1 - \frac{C_0(\boldsymbol{\omega}, t)}{\delta K} \right).$$

A solvability condition for λ_2 (Garlick et al., 2011) requires the non-homogeneous terms (terms *not* involving λ_2) integrate to zero on scales larger than $\boldsymbol{s}$. Following Yurk and Cobbold (2018) and Maciel and Lutscher (2018), we integrate over a region, Ω, which is intermediate in scale between $\boldsymbol{s}$ and $\boldsymbol{\omega}$. This integration leads to the *homogenized* equation for C_0,

$$\frac{\partial}{\partial t}C_0(\boldsymbol{\omega},t) = D(\boldsymbol{\omega})\left(\frac{\partial^2}{\partial\omega_1^2}+\frac{\partial^2}{\partial\omega_2^2}\right)C_0(\boldsymbol{\omega},t)+\gamma C_0(\boldsymbol{\omega},t)\left(1-\frac{C_0(\boldsymbol{\omega},t)}{\tilde{K}(\boldsymbol{\omega})}\right), \tag{7}$$

where the *homogenized* diffusion coefficients are

$$D(\boldsymbol{\omega}) = \frac{|\Omega|}{\int_\Omega \frac{1}{\delta}d\boldsymbol{s}},$$

and the *homogenized* density-dependence parameters are

$$\tilde{K}(\boldsymbol{\omega}) = \frac{K|\Omega|}{D\int_\Omega \frac{1}{\delta^2}d\boldsymbol{s}},$$

with $|\Omega| = \int_\Omega 1 d\boldsymbol{s}$.

To obtain numerical solutions, we discretized Equation 7 using first-order forward differences in time, and centered differences in space (Wikle, 2003; Zheng and Aukema, 2010; Hooten and Hefley, 2019), such that

$$\begin{aligned}
\frac{\partial}{\partial t}C_0(\boldsymbol{\omega},t) &\approx \frac{C_0(\boldsymbol{\omega},t)-C_0(\boldsymbol{\omega},t-\Delta t)}{\Delta t},\\
\frac{\partial^2}{\partial\omega_1^2}C_0(\boldsymbol{\omega},t) &\approx \frac{C_0(\omega_1+\Delta\omega_1,\omega_2,t)-2C_0(\boldsymbol{\omega},t)+C_0(\omega_1-\Delta\omega_1,\omega_2,t)}{\Delta\omega_1^2},\\
\frac{\partial^2}{\partial\omega_2^2}C_0(\boldsymbol{\omega},t) &\approx \frac{C_0(\omega_1,\omega_2+\Delta\omega_2,t)-2C_0(\boldsymbol{\omega},t)+C_0(\omega_1,\omega_2-\Delta\omega_2,t)}{\Delta\omega_2^2}.
\end{aligned}$$

As a result of applying the above differences, we have

$$
\begin{aligned}
C_0(\boldsymbol{\omega}, t) \approx\ & C_0(\boldsymbol{\omega}, t-\Delta t)\left[1-2D(\boldsymbol{\omega})\left(\frac{\Delta t}{\Delta\omega_1^2}+\frac{\Delta t}{\Delta\omega_2^2}\right)+\gamma\Delta t\right] \\
& + C_0(\omega_1-\Delta\omega_1, \omega_2, t-\Delta t)\left[\frac{\Delta t}{\Delta\omega_1^2}D(\boldsymbol{\omega})\right] \\
& + C_0(\omega_1+\Delta\omega_1, \omega_2, t-\Delta t)\left[\frac{\Delta t}{\Delta\omega_1^2}D(\boldsymbol{\omega})\right] \\
& + C_0(\omega_1, \omega_2-\Delta\omega_2, t-\Delta t)\left[\frac{\Delta t}{\Delta\omega_2^2}D(\boldsymbol{\omega})\right] \\
& + C_0(\omega_1, \omega_2+\Delta\omega_2, t-\Delta t)\left[\frac{\Delta t}{\Delta\omega_2^2}D(\boldsymbol{\omega})\right] \\
& - C_0(\boldsymbol{\omega}, t-\Delta t)^2\left(\frac{\gamma}{\tilde{K}(\boldsymbol{\omega})}\Delta t\right). \qquad (8)
\end{aligned}
$$

We rewrite Equation 8 using matrix notation as

$$
\boldsymbol{C}_0(t) \approx \boldsymbol{H}\boldsymbol{C}_0(t-\Delta t) - \boldsymbol{C}_0(t-\Delta t)^2\left(\frac{\gamma}{\tilde{\boldsymbol{K}}}\Delta t\right), \qquad (9)
$$

where $\boldsymbol{H}$ is a propagator matrix with five non-zero entries row-wise, except those related to boundary conditions. The model described in Equation 9 fits into the class of general quadratic nonlinear models developed by Wikle and Hooten (2010).

Solving Equation 7 numerically yields approximate solutions for $\lambda(\boldsymbol{s}, t)$ at the large spatial scale. To retrieve the approximate small scale solutions, we use $\lambda(\boldsymbol{s}, t) \approx C_0(\boldsymbol{\omega}, t)/\delta(\boldsymbol{s})$. Graphical illustrations of the homogenization procedure in our application can be found in Appendix C. The homogenized solution we derived will only apply exactly when consistent initial conditions are given. However, as shown by Garlick et al. (2011), solutions with components not precisely aligned with the homogenization assumptions will decay exponentially rapidly to the homogenized solution, and consequently, associated errors can be safely neglected on the slow temporal scale. Homogenization in two-dimensional space reduces computation complexity by an order of $\mathcal{O}(\epsilon)$ in each spatial dimension, and relaxation

of the numerical stability requirement that temporal discretization scales with the square of spatial discretization further reduces complexity by an order of $\mathcal{O}(\epsilon^2)$. Because $\epsilon \approx 0.1$, our algorithm for solving Equation 4 using homogenization is about 10^4 times faster than solving it without using homogenization.

3. APPLICATION

3.1. Data

To estimate spatio-temporal sea otter abundance in Glacier Bay, and to understand the effect of environmental factors on their population dynamics, we fit our model using data from three different sources of sea otter counts: aerial survey, intensive survey units (ISU), and aerial photographic images.

The aerial survey data were collected during 1993, 1996-2006, 2009, 2010, and 2012, by observers flying in an aircraft at an elevation of 300ft over 400m-wide transects systematically placed across Glacier Bay. Sea otters were counted from the aircraft over contiguous 400m×400m regions.

The ISU data were collected during 1999-2004, 2006, and 2012, using the method developed by Bodkin and Udevitz (1999). During an aerial survey, intensive searches were initiated upon detection of sea otters, by observers flying repeatedly along the circumference of a 400m×400m region until no additional individuals were observed. The ISU data serve as a direct observation of true abundances $\boldsymbol{N}_o$.

The data collected in 2017 and 2018 reflected recent advancements in survey technology, which include using aerial photographic surveys instead of observer-based methods. After the survey, the sea otters in each image were counted by a trained observer. Each image covers a 60m×90m region, with overlap between two consecutive images. To reconcile the spatial scales of data collected during photographic surveys and observer-based surveys,

we assumed homogeneous population intensity within a 400m×400m region, so that the intensity over any 60m×90m sub-region is proportional to the intensity over the 400m×400m region. In addition, we used only non-overlapping images that are conditionally independent samples. Modeling dependence among overlapping images is beyond the scope of this paper; however, see Williams et al. (2017) for a detailed discussion on using image overlap to estimate detection probability. Lastly, we aggregated counts in images belonging to the same 400m×400m region, so that

$$y_{i,t} = \sum_{j=1}^{n_{i,t}} y_{i,j,t} \sim \text{Binom}(N_{i,t},\ p_t),$$

$$N_{i,t} \sim \text{NB}(n_{i,t} A \lambda_{i,t},\ n_{i,t}\tau),$$

where $y_{i,j,t}$ denotes the observed relative abundance in the jth image at site i in year t, $n_{i,t}$ denotes the number of non-overlapping images, and $A = \frac{60\times 90}{400\times 400}$ denotes the ratio between the two survey spatial scales.

3.2. Simulation

We conducted a simulation study to compare our model that includes the logistic reaction component to a model with the Malthusian reaction component, when population dynamics follow density-regulated growth. We denote our hierarchical model outlined in Section 2.1 as the "logistic model," and the model with the same hierarchy but the following process,

$$\frac{\partial}{\partial t}\lambda(\boldsymbol{s}, t) = \left(\frac{\partial^2}{\partial s_1^2} + \frac{\partial^2}{\partial s_2^2}\right)\delta(\boldsymbol{s})\lambda(\boldsymbol{s}, t) + \gamma\lambda(\boldsymbol{s}, t),$$

as the "Malthusian model."

We simulated sea otter population intensities at 400m×400m spatial resolution over Glacier Bay from 1993 to 2018 using the process model in Section 2.1.2. Then, we generated true abundances and relative abundances using the data model in Section 2.1.1. We sampled

relative and true abundances similar to the actual data collection procedure. That is, in each year from 1993 to 2018, we first randomly sampled horizontal strips across Glacier Bay as our transects, where we recorded observed relative abundances, $\boldsymbol{Y}$. Then, we randomly sampled ISU locations from these transects, where we recorded observed true abundances, $\boldsymbol{N}_o$. We summarized the true parameter values and their posterior distributions resulting from the two model fits in Table 1.

[Table 1 about here.]

Table 1 shows that the logistic model was able to capture all true parameter values in their respective 95% credible intervals. On the other hand, the Malthusian model overestimated initial conditions for magnitude and range, and underestimated intrinsic growth rate based on simulated data. The Malthusian model was also unable to provide inference on the density-dependence parameter, K, due to misspecification.

An important quantity derived from spatio-temporal forecasts of sea otter abundance in Glacier Bay is the total abundance through time, $N(t) = \int_{\mathcal{S}} N(\boldsymbol{s}, t) d\boldsymbol{s}$. A sample of total abundance in year t is obtained by

$$N^{(r)}(t) = \sum_{i=1}^{n_{o,t}} N_{i,t} + \sum_{j=1}^{n_t - n_{o,t}} \hat{N}_{j,t}^{(r)} + \sum_{k=1}^{n - n_t} \tilde{N}_{k,t}^{(r)},$$

where $N_{i,t}$ is an observation of true abundance, $\hat{N}_{j,t}^{(r)}$ is a posterior sample of true abundance where relative abundance was observed, and $\tilde{N}_{k,t}^{(r)}$ is a posterior predictive sample of true abundance where no data were observed. Figure 1 indicates that the logistic model was able to capture true total abundances in their respective 95% credible intervals; however, the Malthusian model tended to overestimate abundance after year 2015. This demonstrates the limitation of the Malthusian model when population growth is density regulated. Although the exponential growth curve may mimic the behavior of the logistic growth curve before total abundance reaches the inflection point (possibly by overestimating initial abundance

and underestimating growth rate), it will nonetheless deviate from the truth as population size approaches the asymptote.

[Figure 1 about here.]

3.3. Case Study

We fit our model to the data described in Section 3.1. For homogenization, we defined the small computational scale in space to be 400m×400m, and the large computational scale in space to be 4000m×4000m, at which we solved the discretized PDE in Equation 8. We calculated the homogenized coefficients over areas $\Omega = 6000\text{m} \times 6000\text{m}$ centered on each large-scale cell. The homogenization scale and the small and large computational scales were selected based on previous implementations to balance between desired accuracy and available computational resources. We ran the MCMC algorithm in R version 3.0.2 (R Core Team, 2019) with 15,000 iterations, and used a burn-in of 7,500 and a thinning rate of 1/10. Table 2 summarizes posterior distributions of model parameters. All four coefficients for environmental covariates have 95% credible intervals that did not include zero, suggesting that sea otter diffusion is significantly influenced by habitat. Specifically, high motility is related to deep water, areas away from the shore, steep bottom slopes, and complex shorelines. The posterior mean intrinsic growth rate of 0.24 is close to the estimate reported by Estes (1990), which is reasonable to expect during colonization. Figure 2 shows that the estimated total abundances from our model agreed with the design-based estimates available during 1999-2004, 2006, and 2012 (Bodkin and Udevitz, 1999). Maps of the log of posterior predictive mean abundances and the table summarizing posterior predictive total abundances can be found in Appendix B.

[Table 2 about here.]

[Figure 2 about here.]

To demonstrate that the logistic model improves forecasts of sea otter abundance in Glacier Bay, we conducted a 5-fold cross-validation using the posterior predictive score (Gelman et al., 2014; Hooten and Hobbs, 2015)

$$\sum_{m=1}^{M} \log\left(\frac{\sum_{r=1}^{R}[\boldsymbol{N}_o^m|\boldsymbol{Y},\boldsymbol{N}_o^{-m},\boldsymbol{\theta}^{(t)}]}{R}\right),$$

where $\boldsymbol{N}_o^m$ and $\boldsymbol{N}_o^{-m}$ are the observed true abundances for validation and training in the mth fold, respectively. The vector $\boldsymbol{\theta}^{(r)} = \left(\boldsymbol{p}^{(r)}, \tau^{(r)}, \boldsymbol{\beta}^{(r)}, \theta^{(r)}, \kappa^{(r)}, \gamma^{(r)}, K^{(r)}\right)$ is the rth posterior sample of parameters. The score for the logistic model (-2880) showed an improvement in forecast ability over the score for the Malthusian model (-2896).

The logistic model also allowed us to investigate the equilibrium abundance of sea otters in Glacier Bay. Population dynamics at equilibrium satisfy $\frac{\partial}{\partial t}\lambda(\boldsymbol{s},t) = 0$, and we can determine the state of equilibrium numerically using posterior predictive samples of abundances, such that for $0 < u \ll 1$,

$$\left|\frac{1}{R}\sum_{r=1}^{R}\left(\tilde{N}_{k,t_e}^{(r)} - \tilde{N}_{k,t_e-\Delta t}^{(r)}\right)\right| < u, \text{ for } k = 1,\ldots,n.$$

We denote T_e, the smallest t_e that satistfies the above condition, as the time of equilibrium. In our case study, we found $T_e = 2050$ to provide an acceptable approximation. Alternatively, because analytical solutions to Equation 7, $C_0(\boldsymbol{\omega},t)$, converges to $\tilde{K}(\boldsymbol{\omega})$ away from boundaries as t goes to infinity, the homogenization procedure suggests that $\lambda(\boldsymbol{s},T_e) \approx \tilde{K}(\boldsymbol{\omega})/\delta(\boldsymbol{s})$ at system equilibrium. Therefore, we obtained a posterior predictive realization of local equilibrium abundance by sampling from the predictive full-conditional distribution,

$$\tilde{N}_{k,T_e}^{(r)} \sim \text{NB}\left(\frac{\tilde{K}^{(r)}(\boldsymbol{\omega})}{\delta^{(r)}(\boldsymbol{s})}, \tau^{(r)}\right).$$

We mapped mean equilibrium abundances with associated uncertainties in Figure 3. Our analysis shows that, while K may be perceived as a parameter that regulates local

abundance through intraspecific competition, local abundance at equilibrium is not bounded by K (Yurk and Cobbold, 2018). The solution to $\frac{\partial}{\partial t}\lambda\left(\boldsymbol{s}, T_e\right) = 0$ leads to the equation $\frac{\gamma}{K}\lambda\left(\boldsymbol{s}, T_e\right)\left(K - \lambda\left(\boldsymbol{s}, T_e\right)\right) = \left(\frac{\partial^2}{\partial s_1^2} + \frac{\partial^2}{\partial s_2^2}\right)\delta(\boldsymbol{s})\lambda\left(\boldsymbol{s}, T_e\right)$, and $\lambda\left(\boldsymbol{s}, T_e\right)$ will exceed K when the second derivatives on the right hand side are negative.

Further, we refer to the total abundance at equilibrium as the "effective carrying capacity," and it is unlikely to reach the "nominal carrying capacity" obtained by integrating K over the study area (Figure 4). When diffusion coefficients are constant in space, the local equilibrium intensities will approach K asymptotically, and the effective carrying capacity will converge to the nominal carrying capacity in probability. However, when diffusion coefficients are spatially heterogeneous, Jensen's inequality implies that

$$\frac{\tilde{K}(\boldsymbol{\omega})}{D(\boldsymbol{\omega})} = \frac{K|\Omega|}{\int_\Omega \frac{1}{\delta^2} d\boldsymbol{s}} \cdot \left(\frac{1}{|\Omega|}\int_\Omega \frac{1}{\delta} d\boldsymbol{s}\right)^2 < \frac{K}{\left(\int_\Omega \frac{1}{\delta} d\boldsymbol{s}\right)^2} \cdot \left(\int_\Omega \frac{1}{\delta} d\boldsymbol{s}\right)^2 = K,$$

and because $C_0(\boldsymbol{\omega}, t) \to \tilde{K}(\boldsymbol{\omega})$, we can infer an upper bound on population intensities,

$$\lambda(\boldsymbol{s}, t) \approx \frac{C_0(\boldsymbol{\omega}, t)}{\delta(\boldsymbol{s})} \to \frac{\tilde{K}(\boldsymbol{\omega})}{\delta(\boldsymbol{s})} < \frac{D(\boldsymbol{\omega})K}{\delta(\boldsymbol{s})}.$$

Integrating the above inequality over the entire study domain results in

$$\int_{\mathcal{S}} \lambda\left(\boldsymbol{s}, T_e\right) d\boldsymbol{s} < K \int_{\mathcal{S}} \frac{D(\boldsymbol{\omega})}{\delta(\boldsymbol{s})} d\boldsymbol{s} = K|\mathcal{S}|,$$

which indicates that the mean effective carrying capacity is bounded above by the nominal carrying capacity. In fact, the more spatial variability there exists in $\delta(\boldsymbol{s})$, the further the mean effective carrying capacity will be bounded away from the nominal carrying capacity.

[Figure 3 about here.]

[Figure 4 about here.]

4. DISCUSSION

We demonstrated that using logistic growth in the reaction-diffusion model improved forecast of sea otter abundance in Glacier Bay. The logistic reaction component allowed us to infer spatially-varying local equilibrium abundances, and it also enabled us to study the effect of heterogeneous diffusion on the carrying capacity of the system. Logistic growth is a relatively simple model for population growth that demonstrate long-term equilibrium (Turchin, 2003). One way to extend our model is to modify the reaction component by allowing more complicated population dynamics, such as an Allee effect or multiple population equilibria (Estes, 1990). We are exploring such extensions in ongoing research.

Our model is helpful for understanding the impact of preferential dispersion on system equilibrium, and can be applied to ecological processes beyond colonization. For example, our model can be extended to study dispersal-mediated coexistence of multiple species, where population diffusion and growth are driven by predator-prey interactions (Holmes et al., 1994). Further, learning about spatially-varying local equilibirum abundances over a heterogeneous environment will be important for developing future ecological models of the nearshore benthic food web in Glacier Bay, particularly given the relatively small-scales at which sea otters move, their high site-fidelity, and small home-ranges.

The formulation of a homogenized PDE was essential for model implementation in the Glacier Bay study system associated with our example because it enabled us to obtain inference at a fine spatial resolution with feasible computation time. The homogenized coefficients in the form of harmonic means also provided an alternative way to consider dimension reduction. Although homogenization theory suggests that the small and large spatial scales associated with implementation should be set based on empirical properties (periodicities) of the covariates, in practice, the study system may not be perfectly periodic and the coefficients associated with the influence of the covariates on diffusion are unknown. Thus, the implementation scales are often driven by the availability of data, the amount

of computation resources, and the requirements for inference. Because homogenization uses approximation by power series and the order of approximation error is the same as the ratio of small-to-large spatial scales, faster computation will come at the cost of less accuracy.

Finally, the ongoing collection of aerial imagery provides an incentive for developing statistical sampling methods to optimally combine supervised and unsupervised object classification approaches (Seymour et al., 2017). It also motivates the development of a statistically rigorous georectification procedure, whose uncertainty will be measured in a hierarchical framework, so that we can better account for replications and detectabilities using image overlaps.

ACKNOWLEDGEMENTS

This project was funded by National Park Service Inventory and Monitoring Program, Glacier Bay National Park Marine Management Fund, and NSF DMS 1614392. Any use of trade, firm, or product names is for descriptive purposes only and does not imply endorsement by the U.S. Government. Observer-based data were collected by George Esslinger, Ben Weitzman, Dan Monson, Janet Neilson, Andy Harcombe, Pat Kearney, Mike Sharp, Chuck Schroth, and Steve Wilson. Louise Taylor-Thomas, Dennis Lozier, Desmond Kiesel, and William Johnson assisted with aerial photographic surveys, logistics, and data management. The authors also thank James Bodkin, Heather Colletti, Tom Edwards, George Esslinger, Marti Garlick, Dan Monson, Dan Esler, and Ian McGahan for valuable insights related to this research.

REFERENCES

Banerjee, S., Carlin, B. P., and Gelfand, A. E. (2004). *Hierarchical Modeling and Analysis for Spatia Data.* Chapman and Hall/CRC, Boca Raton, Florida, USA.

Berliner, L. M. (1996). Hierarchical Bayesian time series models. In *Maximum Entropy and Bayesian Methods*, pages 15–22. Springer, New York, New York, USA.

Bodkin, J. L. and Udevitz, M. S. (1999). An aerial survey method to estimate sea otter abundance. *Marine Mammal Survey and Assessment Methods. Balekema, Rotterdam, Netherlands* pages 13–26.

Cantrell, R. S. and Cosner, C. (2004). *Spatial Ecology via Reaction-Diffusion Equations.* John Wiley & Sons, Chichester, UK.

Cressie, N. and Wikle, C. K. (2011). *Statistics for Spatio-Temporal Data.* John Wiley & Sons, Hoboken, New Jersey, USA.

Estes, J. A. (1990). Growth and equilibrium in sea otter populations. *Journal of Animal Ecology* **59,** 385–401.

Garlick, M. J., Powell, J. A., Hooten, M. B., and McFarlane, L. R. (2011). Homogenization of large-scale movement models in ecology. *Bulletin of Mathematical Biology* **73,** 2088–2108.

Gelman, A., Huang, J., and Vehtari, A. (2014). Understanding predictive information criteria for Bayesian models. *Statistics and Computing* **24,** 997–1016.

Hefley, T. J., Hooten, M. B., Russel, R. E., Walsh, D. P., and Powell, J. A. (2017). When mechanism matters: Bayesian forecasting using models of ecological diffusion. *Ecology Letters* **20,** 640–650.

Hilborn, R. and Mangel, M. (1997). *The Ecological Detective: Confronting Models with Data.* Princeton University Press, Princeton, New Jersey, USA.

Hobbs, N. T. and Hooten, M. B. (2015). *Bayesian Models: A Statistical Primer for Ecologists.* Princeton University Press, Princeton, New Jersey, USA.

Holmes, E. E., Lewis, M. A., Banks, J., and Veit, R. (1994). Partial differential equations in ecology: spatial interactions and population dynamics. *Ecology* **75,** 17–29.

Holmes, M. H. (2013). *Introduction to Perturbation Methods (Second Edition).* Springer, New York, New York, USA.

Hooten, M. B., Garlick, M. J., and Powell, J. A. (2013). Computationally efficient statistical differential equation modeling using homogenization. *Journal of Agricultural, Biological, and Environmental Statistics* **18,** 405–428.

Hooten, M. B. and Hefley, T. J. (2019). *Bringing Bayesian Models to Life.* Chapman and Hall/CRC.

Hooten, M. B. and Hobbs, N. (2015). A guide to Bayesian model selection for ecologists. *Ecological Monographs* **85,** 3–28.

Hooten, M. B. and Wikle, C. K. (2008). A hierarchical Bayesian non-linear spatio-temporal model for the spread of invasive species with application to the Eurasian Collard-Dove. *Environmental and Ecological Statistics* **15,** 59–70.

Jameson, R. J. (1989). Movements, home range, and territories of male sea otters off central California. *Marine Mammal Science* **5,** 159–172.

Larson, S. E., Bodkin, J. L., and VanBlaricom, G. R. (2014). *Sea otter conservation*. Academic Press.

Maciel, G. A. and Lutscher, F. (2018). Movement behavior determines competitive outcome and spread rates in strongly heterogeneous landscapes. *Theoretical Ecology* **11,** 351–365.

Powell, J. A. and Zimmermann, N. E. (2004). Multiscale analysis of active seed dispersal contributes to resolving Reid's paradox. *Ecology* **85,** 490–506.

R Core Team (2019). *R: A language and environment for statistical computing*. R Foundation for Statistical Computing, Vienna, Austria.

Risken, H. (1989). *The Fokker-Planck Equation: Methods of Solution and Applications*. Springer, New York, New York, USA.

Royle, A. J. (2004). N-mixture models for estimating population size from spatially replicated counts. *Biometrics* **60,** 108–115.

Seymour, A. C., Dale, J., Hammill, M., Halpin, P. N., and Johnston, D. W. (2017). Automated detection and enumeration of marine wildlife using unmanned aircraft systems (UAS) and thermal imagery. *Scientific Reports* **7,** 45127.

Turchin, P. (1998). *Quantitative Analysis of Movement*. Sinauer Associates, Inc. Publishers, Sunderland, Massachusetts, USA.

Turchin, P. (2003). *Complex Population Dynamics: A Theoretical/Empirical Synthesis*. Princeton University Press, Princeton, New Jersey, USA.

Ver Hoef, J. M. and Boveng, P. L. (2007). Quasi-Poisson vs. negative binomial regression: how should we model overdispersed count data? *Ecology* **88,** 2766–2772.

Wikle, C. K. (2003). Hierarchical Bayesian models for predicting the spread of ecological processes. *Ecology* **84,** 1382–1394.

Wikle, C. K. and Hooten, M. B. (2010). A general science-based framework for predicting the spread of ecological processes. *Test* **19,** 417–451.

Williams, P. J., Hooten, M. B., Esslinger, G. G., Womble, J. N., Bodkin, J. L., and Bower, M. R. (2019). The rise of an apex predator following deglaciation. *Diversity and Distribution* **25,** 895–908.

Williams, P. J., Hooten, M. B., Womble, J. N., and Bower, M. R. (2017). Estimating occupancy and abundance using aerial images with imperfect detection. *Methods in Ecology and Evolution* **8,** 1679–1689.

Williams, P. J., Hooten, M. B., Womble, J. N., Esslinger, G. G., Bower, M. R., and Hefley, T. J. (2017). An integrated data model to estimate spatiotemporal occupancy, abundance, and colonization dynamics. *Ecology* **98,** 328–336.

Yurk, B. P. and Cobbold, C. A. (2018). Homogenization techniques for population dynamics in strongly heterogeneous landscapes. *Journal of Biological Dynamics* **12,** 171–193.

Zheng, Y. and Aukema, B. H. (2010). Hierarchical dynamic modeling of outbreaks of mountain pine beetle using partial differential equations. *Environmetrics* **21,** 801–816.

APPENDIX A: PRIOR DISTRIBUTIONS

$[p_t] = \text{Beta}(30, 10)$ for $t = 1, \ldots, T$

$[\boldsymbol{\beta}] = \text{N}(\mathbf{0}, 10^2\boldsymbol{I})$

$[\theta] = \text{TN}(100, 200^2)_0^\infty$

$[\kappa] = \text{TN}(10, 100^2)_0^\infty$

$[\gamma] = \text{Unif}(0, 0.5)$

$[K] = \text{Unif}(0, 100)$

$[\tau] = \text{Unif}(0, 1)$

APPENDIX B: SUMMARY OF POSTERIOR PREDICTIVE ABUNDANCES FOR THE SEA OTTER CASE STUDY

Table 3 summarizes the posterior predictive distributions of the total sea otter abundances in Glacier Bay, Alaska, from 1993 to 2018.

[Table 3 about here.]

Figure 5 maps the log of posterior predictive mean sea otter abundances in Glacier Bay, Alaska, from 1993 to 2018.

[Figure 5 about here.]

APPENDIX C: GRAPHICAL ILLUSTRATIONS OF HOMOGENIZATION

Figure 6 illustrates the three computational scales in the homogenization procedure.

[Figure 6 about here.]

Figure 7 gives an example of the original and homogenized surfaces during one MCMC iteration.

[Figure 7 about here.]

APPENDIX D: MARKOV CHAIN MONTE CARLO ALGORITHM FOR PARAMETER ESTIMATION

1. Define initial values for $\boldsymbol{\beta}^{(0)}$, $\gamma^{(0)}$, $K^{(0)}$, $\theta^{(0)}$, $\kappa^{(0)}$, $\tau^{(0)}$, and $\boldsymbol{p}^{(0)}$.
2. Initialize population intensity surface $\boldsymbol{\lambda}^{(0)}$ and true abundance $N_{i,t}^{(0)}$ where not observed:
   (a) Calculate the diffusion surface, $\boldsymbol{\delta}^{(0)} = \exp\left(\boldsymbol{X}\boldsymbol{\beta}^{(0)}\right)$.
   (b) Calculate the homogenized diffusion coefficients, $D(\boldsymbol{\omega})$. From this point on, spatial indices will be used with subscripts to imply discretization. For each grid cell $\boldsymbol{\omega}_j$ at the large computation scale, let the homogenization region Ω_j be centered at $\boldsymbol{\omega}_j$ and consist of c^2 grid cells, $\boldsymbol{s}_i$, at the small computation scale. Let c be slightly larger than $1/\epsilon$. Then, $D(\boldsymbol{\omega}_j)^{(0)} = \frac{c^2}{\sum_{\boldsymbol{s}_i \in \Omega_j} 1/\delta(\boldsymbol{s}_i)^{(0)}}$.
   (c) Calculate the homogenized density dependence parameters, $\tilde{K}(\boldsymbol{\omega}_j)^{(0)} = \frac{K^{(0)} c^2}{D(\boldsymbol{\omega}_j)^{(0)} \sum_{\boldsymbol{s}_i \in \Omega_j} 1/\delta^2(\boldsymbol{s}_i)^{(0)}}$.
   (d) Calculate the propagator matrix $\boldsymbol{H}^{(0)}$ as described in Equation 8.
   (e) Calculate $C_0(\boldsymbol{\omega}_j, 0)^{(0)} = \frac{\theta^{(0)} \exp\left(-\frac{|\boldsymbol{\omega}_j - \boldsymbol{s}_d|^2}{\kappa^{2(0)}}\right)}{\sum_{\boldsymbol{s}_i \in \mathcal{S}} \exp\left(-\frac{|\boldsymbol{s}_i - \boldsymbol{s}_d|^2}{\kappa^{2(0)}}\right)}$, and propagate the homogenized solutions, $\boldsymbol{C}_0(t)^{(0)} = \boldsymbol{H}^{(0)}\boldsymbol{C}_0(t-1)^{(0)} - \boldsymbol{C}_0^2(t-1)^{(0)} \frac{\gamma^{(0)}}{\tilde{\boldsymbol{K}}^{(0)}}$ for $t = 2, \ldots, T$.
   (f) Retrieve the original solutions, $\lambda_{i,t}^{(0)} = C_0(\boldsymbol{\omega}_j, t)/\delta(\boldsymbol{s}_i)$, where $\boldsymbol{s}_i \in \mathcal{A}(\boldsymbol{\omega}_j)$.
   (g) If true abundance is not observed at $\boldsymbol{s}_i$ in year t, sample $N_{i,t}^{(0)} \sim \text{NB}\left(\lambda_{i,t}^{(0)}, \tau^{(0)}\right)$; otherwise, fix $N_{i,t}$ to be the observed value.
3. Set $k = 1$
4. Update $\beta_r^{(k-1)}$ for r = 0, ..., 4 using Metropolis-Hastings. Sample $\beta_r^{(*)} \sim \text{N}\left(\beta_r^{(k-1)}, \sigma^2_{\beta,\text{tune}}\right)$. Calculate the new propagator matrix $\boldsymbol{H}^{(*)}$ following Steps 2(a) -

(d), and then calculate the Metropolis-Hastings ratio as

$$mh_{\beta_r} = \left(\frac{\prod_{i=1}^{n_t} \prod_{t=1}^{T} \text{NB}\left(N_{i,t}^{(k-1)}; \lambda_{i,t}^{(*)}, \tau^{(k-1)}\right)}{\prod_{i=1}^{n_t} \prod_{t=1}^{T} \text{NB}\left(N_{i,t}^{(k-1)}; \lambda_{i,t}^{(k-1)}, \tau^{(k-1)}\right)} \right) \times \left(\frac{\text{N}\left(\beta_r^{(*)}; \mu_\beta, \sigma_\beta^2\right)}{\text{N}\left(\beta_r^{(k-1)}; \mu_\beta, \sigma_\beta^2\right)} \right).$$

If $mh_{\beta_r} > u$, where $u \sim \text{Unif}(0,1)$, let $\beta_r^{(k)} = \beta_r^{(*)}$ and update $\boldsymbol{\lambda}^{(k-1)} = \boldsymbol{\lambda}^{(*)}$; otherwise, let $\beta_r^{(k)} = \beta_r^{(k-1)}$.

5. Update $\gamma^{(k-1)}$ using Metropolis-Hastings. Sample $\gamma^{(*)} \sim \text{N}\left(\gamma^{(k-1)}, \sigma_{\gamma,\text{tune}}^2\right)$. If $\gamma^{(*)} \in [0, 0.5]$, calculate the new propagator matrix and solve for $\boldsymbol{\lambda}^{(*)}$ following Steps 2(d) - (f). Calculate the Metropolis-Hastings ratio as

$$mh_\gamma = \frac{\prod_{i=1}^{n_t} \prod_{t=1}^{T} \text{NB}\left(N_{i,t}^{(k-1)}; \lambda_{i,t}^{(*)}, \tau^{(k-1)}\right)}{\prod_{i=1}^{n_t} \prod_{t=1}^{T} \text{NB}\left(N_{i,t}^{(k-1)}; \lambda_{i,t}^{(k-1)}, \tau^{(k-1)}\right)}.$$

If $mh_\gamma > u$, where $u \sim \text{Unif}(0,1)$, let $\gamma^{(k)} = \gamma^{(*)}$ and update $\boldsymbol{\lambda}^{(k-1)} = \boldsymbol{\lambda}^{(*)}$; otherwise, let $\gamma^{(k)} = \gamma^{(k-1)}$.

6. Update $K^{(k-1)}$ using Metropolis-Hastings. Sample $K^{(*)} \sim \text{N}\left(K^{(k-1)}, \sigma_{K,\text{tune}}^2\right)$. If $K^{(*)} \in [0, 100]$, calculate the new homogenized density dependence parameters and solve for $\boldsymbol{\lambda}^{(*)}$ following Steps 2(c) - (f). Calculate the Metropolis-Hastings ratio as

$$mh_K = \frac{\prod_{i=1}^{n_t} \prod_{t=1}^{T} \text{NB}\left(N_{i,t}^{(k-1)}; \lambda_{i,t}^{(*)}, \tau^{(k-1)}\right)}{\prod_{i=1}^{n_t} \prod_{t=1}^{T} \text{NB}\left(N_{i,t}^{(k-1)}; \lambda_{i,t}^{(k-1)}, \tau^{(k-1)}\right)}.$$

If $mh_K > u$, where $u \sim \text{Unif}(0,1)$, let $K^{(k)} = K^{(*)}$ and update $\boldsymbol{\lambda}^{(k-1)} = \boldsymbol{\lambda}^{(*)}$; otherwise, let $K^{(k)} = K^{(k-1)}$.

7. Update $\theta^{(k-1)}$ using Metropolis-Hastings. Sample $\theta^{(*)} \sim \text{N}\left(\theta^{(k-1)}, \sigma_{\theta,\text{tune}}^2\right)$. If $\theta^{(*)} > 0$, calculate the new initial conditions and solve for $\boldsymbol{\lambda}^{(*)}$ following Step 2(e). Calculate the

Metropolis-Hastings ratio as

$$mh_\theta = \left(\frac{\prod_{i=1}^{n_t} \prod_{t=1}^{T} \text{NB}\left(N_{i,t}^{(k-1)}; \lambda_{i,t}^{(*)}, \tau^{(k-1)}\right)}{\prod_{i=1}^{n_t} \prod_{t=1}^{T} \text{NB}\left(N_{i,t}^{(k-1)}; \lambda_{i,t}^{(k-1)}, \tau^{(k-1)}\right)} \right) \times \left(\frac{\text{TN}\left(\theta^{(*)}; \mu_\theta, \sigma_\theta^2\right)_0^\infty}{\text{TN}\left(\theta^{(k-1)}; \mu_\theta, \sigma_\theta^2\right)_0^\infty} \right).$$

If $mh_\theta > u$, where $u \sim \text{Unif}(0,1)$, let $\theta^{(k)} = \theta^{(*)}$ and update $\boldsymbol{\lambda}^{(k-1)} = \boldsymbol{\lambda}^{(*)}$; otherwise, let $\theta^{(k)} = \theta^{(k-1)}$.

8. Update $\kappa^{(k-1)}$ using Metropolis-Hastings. Sample $\kappa^{(*)} \sim \text{N}\left(\kappa^{(k-1)}, \sigma_{\kappa,\text{tune}}^2\right)$. If $\kappa^{(*)} > 0$, calculate the new initial conditions and solve for $\boldsymbol{\lambda}^{(*)}$ following Step 2(e). Calculate the Metropolis-Hastings ratio as

$$mh_\kappa = \left(\frac{\prod_{i=1}^{n_t} \prod_{t=1}^{T} \text{NB}\left(N_{i,t}^{(k-1)}; \lambda_{i,t}^{(*)}, \tau^{(k-1)}\right)}{\prod_{i=1}^{n_t} \prod_{t=1}^{T} \text{NB}\left(N_{i,t}^{(k-1)}; \lambda_{i,t}^{(k-1)}, \tau^{(k-1)}\right)} \right) \times \left(\frac{\text{TN}\left(\kappa^{(*)}; \mu_\kappa, \sigma_\kappa^2\right)_0^\infty}{\text{TN}\left(\kappa^{(k-1)}; \mu_\kappa, \sigma_\kappa^2\right)_0^\infty} \right).$$

If $mh_\kappa > u$, where $u \sim \text{Unif}(0,1)$, let $\kappa^{(k)} = \kappa^{(*)}$ and update $\boldsymbol{\lambda}^{(k)} = \boldsymbol{\lambda}^{(*)}$; otherwise, let $\kappa^{(k)} = \kappa^{(k-1)}$.

9. Update $\tau^{(k-1)}$ using Metropolis-Hastings. Sample $\tau^{(*)} \sim \text{N}\left(\tau^{(k-1)}, \sigma_{\tau,\text{tune}}^2\right)$. If $\tau^{(*)} \in [0,1]$, calculate the Metropolis-Hastings ratio as

$$mh_\tau = \frac{\prod_{i=1}^{n_t} \prod_{t=1}^{T} \text{NB}\left(N_{i,t}^{(k-1)}; \lambda_{i,t}^{(k)}, \tau^{(*)}\right)}{\prod_{i=1}^{n_t} \prod_{t=1}^{T} \text{NB}\left(N_{i,t}^{(k-1)}; \lambda_{i,t}^{(k)}, \tau^{(k-1)}\right)}.$$

If $mh_\tau > u$, where $u \sim \text{Unif}(0,1)$, let $\tau^{(k)} = \tau^{(*)}$; otherwise, let $\tau^{(k)} = \tau^{(k-1)}$.

10. Update $p_t^{(k-1)}$ using Gibbs sampling for years when true abundances were observed:

$$p_t^{(k)} \sim \text{Beta}\left(\sum_{i \in \boldsymbol{n}_{o,t}} y_{i,t} + a_p, \sum_{i \in \boldsymbol{n}_{o,t}} (N_{i,t} - y_{i,t}) + b_p \right),$$

where $\boldsymbol{n}_{o,t}$ is a vector of cell indices where true abundances were observed in year t. If no true abundance was observed in year t, let $p_t^{(k)} = p_t^{(k-1)}$.

11. Update $\boldsymbol{N}^{(k-1)}$:

    (a) If relative abundance $y_{i,t}$ was observed, update $N_{i,t}^{(k-1)}$ using Metropolis-Hastings. Sample $N_{i,t}^{(*)} \sim \text{Pois}\left(N_{i,t}^{(k-1)} + 0.5\right)$. Calculate the Metropolis-Hastings ratio as

$$mh_n = \left(\frac{\text{Binom}\left(y_{i,t}; N_{i,t}^{(*)}, p_t^{(k)}\right)}{\text{Binom}\left(y_{i,t}; N_{i,t}^{(k-1)}, p_t^{(k)}\right)}\right) \times \left(\frac{\text{NB}\left(N_{i,t}^{(*)}; \lambda_{i,t}^{(k)}, \tau^{(k)}\right)}{\text{NB}\left(N_{i,t}^{(k-1)}; \lambda_{i,t}^{(k)}, \tau^{(k)}\right)}\right) \times \left(\frac{\text{Pois}\left(N_{i,t}^{(k-1)}; N_{i,t}^{(*)} + 0.5\right)}{\text{Pois}\left(N_{i,t}^{(*)}; N_{i,t}^{(k-1)} + 0.5\right)}\right).$$

    If $mh_n > u$, where $u \sim \text{Unif}(0,1)$, let $N_{i,t}^{(k)} = N_{i,t}^{(*)}$; otherwise, let $N_{i,t}^{(k)} = N_{i,t}^{(k-1)}$.

    (b) If relative abundance $y_{i,t}$ was not observed, sample $N_{i,t}^{(k)}$ from its posterior predictive distribution $\text{NB}\left(\lambda_{i,t}^{(k)}, \tau^{(k)}\right)$.

12. Save $\boldsymbol{\beta}^{(k)}$, $\gamma^{(k)}$, $K^{(k)}$, $\theta^{(k)}$, $\kappa^{(k)}$, $\tau^{(k)}$, $\boldsymbol{p}^{(k)}$, $\boldsymbol{\lambda}^{(k)}$, and $\boldsymbol{N}^{(k)}$.

13. Set $k = k + 1$ and return to Step 4. Iterate the algorithm through Steps 4 to 12 until the sample size is large enough to approximate the posterior distributions.

FIGURES

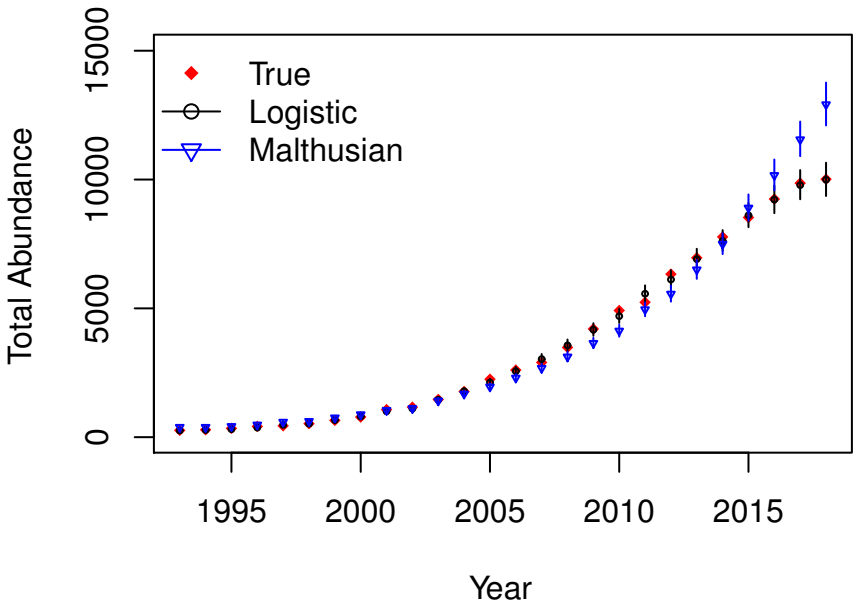

Figure 1. Estimated posterior predictive means and 95% credible intervals for total abundances, $N(t)$, from the logistic and the Malthusian models, overlaid with true total abundances, for the simulated data.

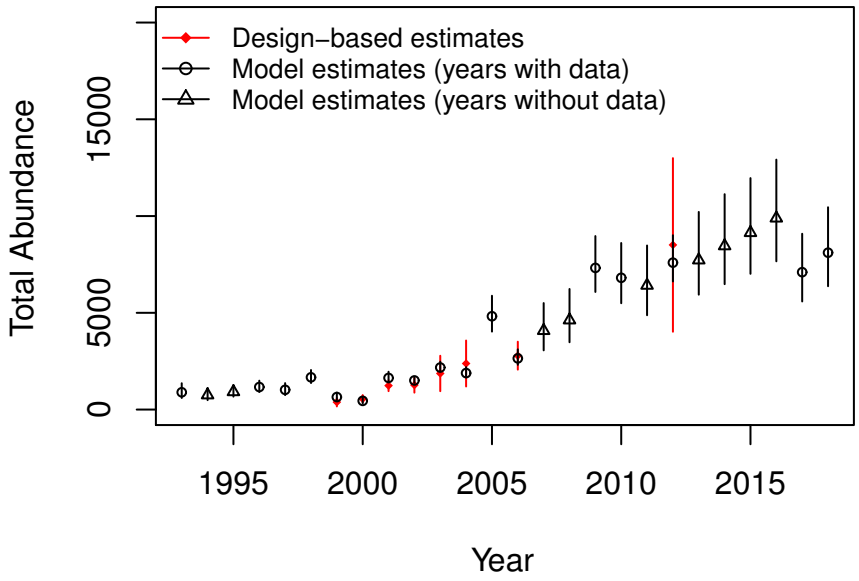

Figure 2. Estimated posterior predictive mean total abundances, $N(t)$, and their 95% credible intervals, overlaid with design-based estimates and their uncertainties, for the sea otter case study.

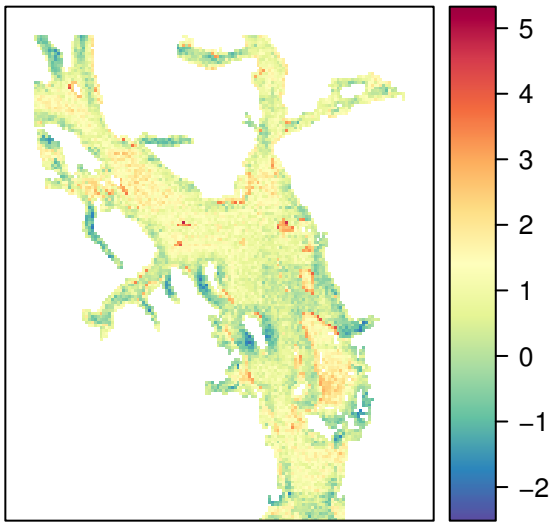

(a)

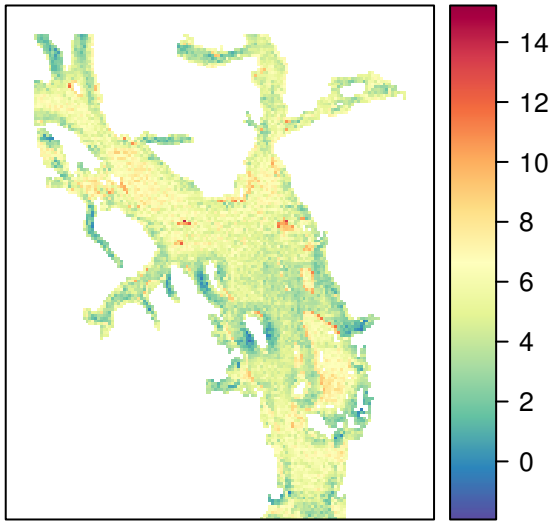

(b)

Figure 3. (a) Log of estimated posterior predictive mean equilibrium abundances, $\tilde{N}_{k,T_e}$, for the sea otter case study. (b) Log of estimated posterior predictive equilibrium variance for the sea otter case study.

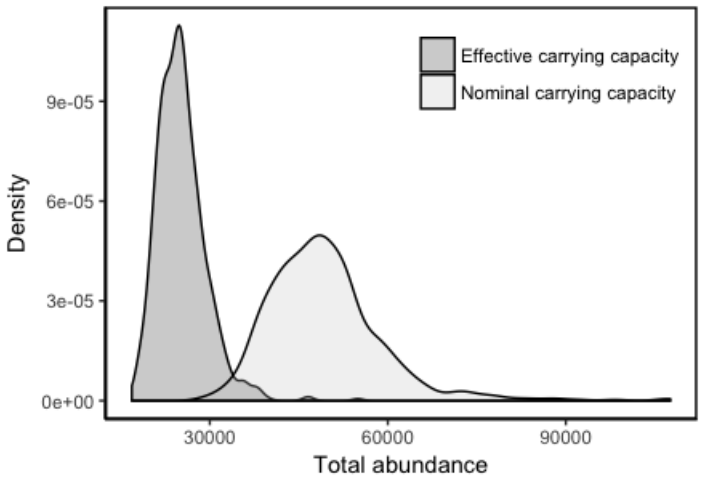

Figure 4. Posterior predictive distributions of the effective carrying capacity, $N(T_e)$, versus the nominal carrying capacity, $K|\mathcal{S}|$, for the sea otter case study.

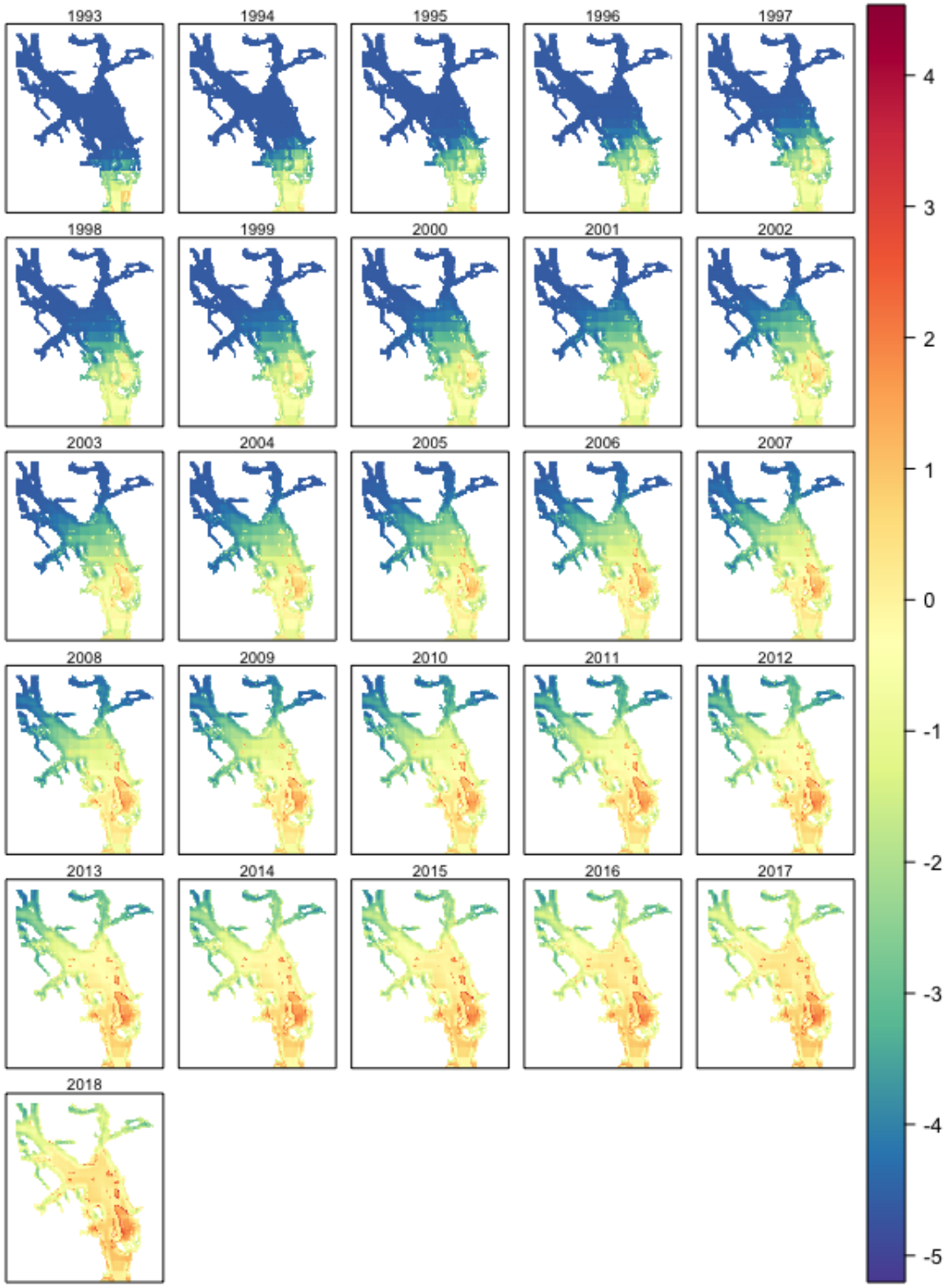

Figure 5. Log of estimated posterior predictive mean sea otter abundances, $N_{i,t}$, in Glacier Bay, from 1993 to 2018.

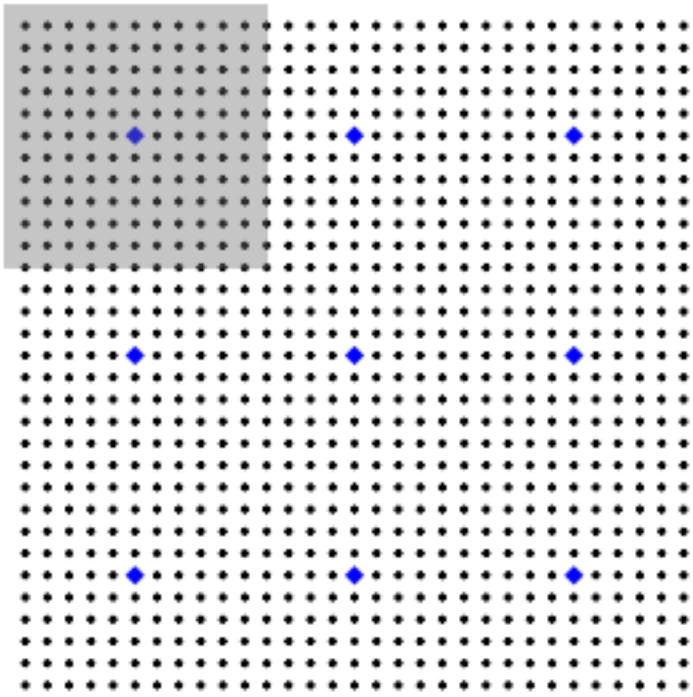

Figure 6. Different scales in homogenization: the black dots represent the small scale spatial variables, $\boldsymbol{s}$, and the blue diamonds represent the large scale spatial variables, $\boldsymbol{\omega}$. The homogenized coefficients associated with each large scale spatial variable are obtained over a homogenization region, Ω, centered at that variable, as is demonstrated by the gray box for the top left blue diamond.

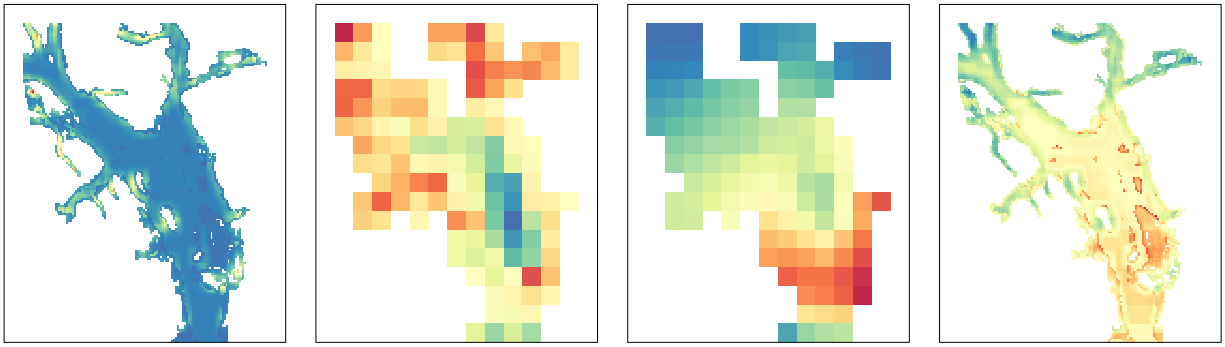

(a) **(b)** **(c)** **(d)**

Figure 7. This series of figures from left to right conceptually illustrate the homogenization surfaces at one time point, t, in one MCMC iteration. In (a) we have the small scale diffusion coefficients, $\delta(\boldsymbol{s})$, from which we obtain the homogenized diffusion coeficients, $D(\boldsymbol{\omega})$, in (b). We then solve the homogenized PDE and map the large scale solutions, $C_0(\boldsymbol{\omega}, t)$, in (c), and finally in (d) we obtain the small scale solutions, $\lambda(\boldsymbol{s}, t)$, to the original PDE by $C_0(\boldsymbol{\omega}, t)/\delta(\boldsymbol{s})$.

TABLES

Parameter	True	Logistic	Malthusian
τ (dispersion)	0.5	0.49 (0.47, 0.51)	0.48 (0.46, 0.50)
β_0 (intercept)	18	17.95 (17.59, 18.29)	18.12 (17.61, 18.55)
β_1 (depth)	-1.5	-1.49 (-1.54, -1.43)	-1.52 (-1.57, -1.47)
β_2 (distance to shore)	0.8	0.76 (0.72, 0.80)	0.75 (0.72, 0.79)
β_3 (bottom slope)	-0.3	-0.29 (-0.34, -0.24)	-0.29 (-0.34, -0.23)
β_4 (shoreline complexity)	1	0.97 (0.93, 1.01)	0.98 (0.94, 1.01)
θ (magnitude)	500	467 (412, 517)	786 (728, 845)
κ (range)	60	60 (47, 74)	81 (67, 98)
γ (growth rate)	0.25	0.25 (0.24, 0.26)	0.18 (0.17, 0.19)
K (density dependence)	5	4.79 (4.25, 5.38)	-

Table 1. True parameter values and estimated posterior means (95% credible intervals) from the logistic and the Malthusian models, for the simulated data.

Parameter	Posterior Mean	95% CI
τ (dispersion)	0.032	(0.030, 0.034)
β_0 (intercept)	16.09	(15.91, 16.32)
β_1 (depth)	-1.12	(-1.30, -0.95)
β_2 (distance to shore)	0.18	(0.08, 0.27)
β_3 (bottom slope)	-0.79	(-0.91, -0.64)
β_4 (shoreline complexity)	0.81	(0.71, 0.91)
θ (magnitude)	649	(515, 801)
κ (range)	8.07	(7.07, 9.19)
γ (growth rate)	0.25	(0.23, 0.27)
K (carrying capacity)	6.12	(4.41, 8.74)

Table 2. Estimated posterior means and 95% credible intervals of model parameters, for the sea otter case study.

Total Abundance (Year)	Posterior Predictive Mean	95% CI
$N(1993)$	893	(599, 1363)
$N(1994)$	749	(485, 1112)
$N(1995)$	915	(667, 1251)
$N(1996)$	1165	(907, 1495)
$N(1997)$	1020	(746, 1367)
$N(1998)$	1667	(1371, 2046)
$N(1999)$	647	(488, 878)
$N(2000)$	450	(323, 624)
$N(2001)$	1635	(1408, 1956)
$N(2002)$	1505	(1381, 1683)
$N(2003)$	2174	(1969, 2477)
$N(2004)$	1886	(1659, 2196)
$N(2005)$	4823	(4028, 5882)
$N(2006)$	2646	(2312, 3114)
$N(2007)$	4076	(3060, 5505)
$N(2008)$	4623	(3479, 6232)
$N(2009)$	7321	(6077, 8966)
$N(2010)$	6810	(5495, 8607)
$N(2011)$	6417	(4875, 8479)
$N(2012)$	7592	(6621, 9009)
$N(2013)$	7724	(5937, 10213)
$N(2014)$	8454	(6480, 11131)
$N(2015)$	9138	(7015, 11962)
$N(2016)$	9889	(7661, 12916)
$N(2017)$	7100	(5586, 9086)
$N(2018)$	8108	(6374, 10456)

Table 3. Estimated posterior predictive means and 95% credible intervals of total sea otter abundances, $N(t)$, in Glacier Bay, from 1993 to 2018.